

ACCELERATION OF COSMIC RAYS IN SUPERNOVA SHOCKS: ELEMENTAL SELECTIVITY OF THE INJECTION MECHANISM

ADRIAN HANUSCH,¹ TATYANA V. LISEYKINA,¹ AND MIKHAIL MALKOV²

¹*Institut für Physik, Universität Rostock, 18051 Rostock, Germany*

²*CASS and Department of Physics, University of California, San Diego, La Jolla, California 92093, USA*

(Dated: January 18, 2019)

Submitted to ApJ

ABSTRACT

Precise measurements of galactic cosmic rays revealed a significant difference between the rigidity spectral indices of protons and helium ions. This finding is a notable contrast to the commonly accepted theoretical prediction that supernova remnant (SNR) shocks accelerate protons and helium ions with the same rigidity alike. Most of the earlier explanations for the "paradox" appealed to SNR environmental factors, such as inhomogeneous p/He mixes in the shock upstream medium, variable ionization states of He, or a multi-SNR origin of the observed spectra. The newest observations, however, are in tension with most of them. In this paper, we show by self-consistent hybrid simulations that such special conditions are not vital for the explanation of the cosmic ray rigidity spectra. In particular, our simulations prove that an SNR shock can modify the chemical composition of accelerated cosmic rays by preferentially extracting them from a homogeneous background plasma without additional, largely untestable assumptions. Our results confirm the earlier theoretical predictions of how the efficiency of injection depends on the shock Mach number M . Its increase with the charge-to-mass ratio saturates at a level that grows with M . We have convolved the time-dependent injection rates of protons and helium ions, obtained from the simulations, with a decreasing shock strength over the active life of SNRs. The integrated SNR rigidity spectrum for p/He ratio compares well with the AMS-02 and PAMELA data.

Keywords: cosmic rays, supernova remnants, acceleration of particles, shock waves

1. INTRODUCTION

The PAMELA and AMS-02 measurements (Aguilar et al. 2015; Adriani et al. 2011) indicated a difference $\Delta q \simeq 0.1$ between the rigidity spectral indices of protons and helium ions, put forth earlier by the balloon-born experiment ATIC-2 (Panov et al. 2009). According to observations (Yoon et al. 2011), the scaling shown in Fig. 1 is likely to continue to higher rigidities. These findings challenge the hypothesis of cosmic ray (CR) origin in the supernova remnants (SNR), see e.g., (Bykov et al. 2018), for a recent review.

The leading CR production mechanisms, the first order Fermi or diffusive shock acceleration (DSA), is elec-

tromagnetic in nature (Fermi 1949). The equations of motion of charged particles in arbitrary electric and magnetic fields can be rewritten in terms of particle rigidity $\mathcal{R} = \mathbf{p}c/eZ$, instead of momentum \mathbf{p} :

$$\frac{1}{c} \frac{d\mathcal{R}}{dt} = \mathbf{E}(\mathbf{r}, t) + \frac{\mathcal{R} \times \mathbf{B}(\mathbf{r}, t)}{\sqrt{\mathcal{R}_0^2 + \mathcal{R}^2}}, \quad (1)$$

$$\frac{1}{c} \frac{d\mathbf{r}}{dt} = \frac{\mathcal{R}}{\sqrt{\mathcal{R}_0^2 + \mathcal{R}^2}}. \quad (2)$$

Here $\mathcal{R}_0 = Am_p c^2 / Ze$, with A being the atomic number and m_p the proton mass. The electric, $\mathbf{E}(\mathbf{r}, t)$, and magnetic, $\mathbf{B}(\mathbf{r}, t)$, fields here are completely arbitrary. So, the equations apply not only to the acceleration of CRs in a SNR shock but also to their propagation through the turbulent interstellar medium (ISM) to an observer. Moreover, the propagation includes an eventual escape of the accelerated CRs from the Milky Way.

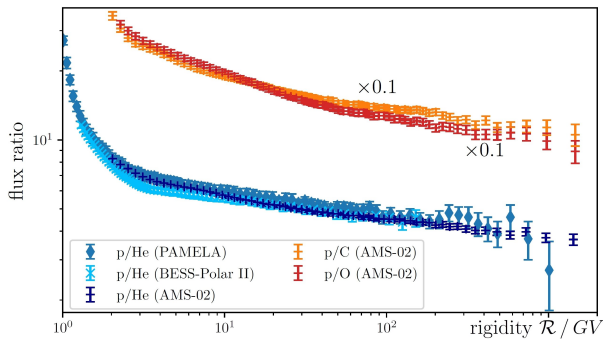


Figure 1. The p/He , p/C , and p/O ratio as a function of particle rigidity. The data is taken from Adriani et al. (2011); Aguilar et al. (2015); Abe et al. (2016); Aguilar et al. (2017).

The equations (1) and (2) show that all species with rigidities $\mathcal{R} \gg \mathcal{R}_0 = Am_p c^2 / Ze$ have nearly identical orbits in the phase space $(\mathbf{r}, \mathcal{R})$. Hence, if different elements enter the acceleration in a *time-independent* ratio at some $\mathcal{R} \gg \mathcal{R}_0 = Am_p c^2 / Ze$, their rigidity spectra in this range should be identical (Malkov et al. 2012; Malkov 2017), in apparent contradiction with ATIC-2, PAMELA, AMS-02 observations, Fig. 1. Note, that at reasonably low rigidities, such as 10 GV and lower, where also solar modulation is observed, the rule of equal rigidity argument does not apply. The reason is that the rest-mass rigidity, $\mathcal{R}_0 \approx 1$ GV for protons, does enter the equations of motion.

To explain the p/He rigidity paradox three ideas have been entertained: (1) shock *evolution in time*; (2) contributions from several SNRs with different p -He mixes and spectral slopes; (3) CR spallation in the ISM that introduces particle sources and sinks in their kinetic equations. Turning to the first idea, assume that the p/He ratio is known at some fiducial rigidity $\mathcal{R} = \mathcal{R}_1 \gg \mathcal{R}_0$. While the shock strength naturally decreases, this ratio must increase at a rate consistent with the observed p/He slope in rigidity. The crucial point here is that the power-law index of shock-accelerated particles decreases with the shock Mach number $M(t)$ rather definitively

$$q = -\frac{d \ln f}{d \ln \mathcal{R}} = \frac{4}{1 - M^{-2}}, \quad (3)$$

where f is the CR distribution function. Therefore, to produce a p/He fixed index at $\mathcal{R} > \mathcal{R}_1$, the p/He ratio at $\mathcal{R} = \mathcal{R}_1$ must depend on $M(t)$ in a specific way. If this dependence is an intrinsic property of collisionless shock, it cannot be adjusted to fit the data, thus making the scenario (1) fully testable. Unlike the scenario (1) above, (2) is not testable because the individual properties of contributing sources are unknown. Besides, it will likely fail the Occam's razor test, especially after the AMS-02 has measured p/C and p/O ratios to be identical to those

of p/He (Aguilar et al. 2017). And moreover, it would be impossible to maintain the spectral slopes in the ratios p/He , p/C and p/O (Aguilar et al. 2017, 2018) nearly constant over an extended rigidity range (Malkov 2017). As for the spallation effects (3), the equivalence between the He, C and O spectra (Aguilar et al. 2018) corroborates the conclusion (Vladimirov et al. 2012) that it is insufficient to explain the observed differences between p and elements whose A/Z values are similar but higher than that of the protons. It follows that the time dependence of the subrelativistic acceleration phase, i.e. injection into DSA, option (1), is the most realistic scenario to consider.

Time dependence of particle acceleration at an SNR shock comes in two flavors. Firstly, the natural shock weakening makes the acceleration time dependent. Secondly, the medium into which the shock propagates may be inhomogeneous (effect of SNR environment) (Ohira & Ioka 2011). If also the background p/He ratio is inhomogeneous and increases outward, after the acceleration it will decrease with rigidity. This is because higher rigidities are dominated by earlier times of acceleration history when the He contribution was higher. The problem with this explanation is that not only the He concentration must decrease with growing shock radius at a specific rate (one free parameter), but so must C and O. This conclusion follows from the newest C/He and O/He AMS-02 flux ratios, which have turned out to be independent of rigidity (Aguilar et al. 2017, 2018). So, He, C, and O are likely to share their acceleration and propagation history. One natural consequence of this is that C and O are unlikely to be preaccelerated from grains, contrary to some earlier suggestions (see (Ohira et al. 2016) for the recent study and earlier references). Note that it is crucial to use the rigidity dependence of the *fractions* of different species as a primary probe into the intrinsic properties of CR accelerators. Unlike the individual spectra, the fractions are unaffected by the CR propagation, reacceleration, and losses from the galaxy, as long as spallation is negligible.

Besides tensions with the recent AMS-02 results, the above-discussed mechanisms require additional and untestable assumptions. To resolve these problems, (Malkov 1998) argued that in quasi-parallel shocks a specific elemental selectivity of the initial phase of the DSA (injection) occurs with no additional assumptions. Analytic calculations have established that the ion injection efficiency into the DSA depends on the shock Mach number, increases with A/Z , and saturates at a level that grows with M . The publication of measurements of p/He ratio by the PAMELA collaboration (Adriani et al. 2011), prompted the authors of (Malkov

et al. 2012) to apply the analytic injection theory to the case $A/Z = 2$ (specifically to He^{2+} , also valid for fully stripped C and O, accurately measured later by AMS-02), producing an excellent fit to the PAMELA data in the relevant rigidity range $2 < \mathcal{R} < 200$ GV. Moreover, the analytic results are largely insensitive to the ionization multiplicity at higher A/Z since the saturation effects becomes significant already at $A/Z \sim 2 - 4$ (see Fig.5 in (Malkov 1998)). Note that lower rigidities are strongly affected by solar modulation, while at higher rigidities the PAMELA statistics was insufficient to make a meaningful comparison.

In this paper we demonstrate that the recent high-precision measurements of elemental spectra with different A/Z are not only consistent with the hypothesis of CR origin in the SNR, but also strongly support it. Although a similar stand has been taken in (Malkov et al. 2012) about the PAMELA findings (Adriani et al. 2011), the new AMS-02 data (Aguilar et al. 2017, 2018) and recent progress in shock simulations allow us to establish crucial missing links in the CR-SNR relation. In particular, the coincidence in accelerated particle spectral slopes of three different elements with $A/Z \simeq 2$ (He, C, and O) discovered by the AMS-02 experiment points to an intrinsic, A/Z -based selection mechanism and rules out incidental ones, such as particle injection from inhomogeneous shock environments, preacceleration of elements locked into grains, or a variable ionization state of He (Serpico 2016). It is important to emphasize here that the latter mechanism was primarily justified by an integrated abundance of different elements, whereas the detailed rigidity spectra have become known only now. On the theoretical side, the p/He calculations (Malkov et al. 2012) are based on an analytic theory (Malkov & Völk 1995) that allows freedom in selecting seed particles for injection. Pre-energized particles evaporating from the shocked downstream plasma back upstream (Parker 1961; Quest 1988) and shock reflected particles (Burgess & Scholer 2015) have been most often discussed. Simulations can remove this uncertainty, thus greatly improving the understanding of the A/Z selectivity mechanism.

Suprathermal protons (shock-reflected, or "evaporating" from hot downstream plasma) drive unstable Alfvén waves in front of the shock. These waves control the injection of all particles by regulating their access to those parts of the phase space from where they can repeatedly cross the shock, thus gaining more energy (Kato 2015; Marcowith et al. 2016). Furthermore, the waves are almost frozen into the local fluid. So, when crossing the shock interface, they trap most particles and prevent them from escaping upstream *again*, thus

significantly reducing their odds for injection. As protons drive these waves, the waves also trap protons most efficiently, while, e.g., He^{2+} have somewhat better chances to escape from the proton-generated waves upstream and to get eventually injected. The trapping becomes naturally stronger with growing wave amplitude, that also grows with the Mach number. This trend is more pronounced for protons than for He ions, which is crucial for the injection selectivity.

Simulations remove another potentially important limitation of the analytic treatment (Malkov et al. 2012). Namely, He ions have not been included in the wave generation upstream and treated only as test-particles. Such approximation is often considered to be sufficient because of the large, $\simeq 10$, p/He number density ratio. However, the He ions drive resonant waves that are typically two times longer than the waves driven by the protons. In the wave-particle interaction, the resonance condition is often more important than the wave amplitude. In addition, the rational relation between the respective wave lengths is suggestive of parametric interactions between them. Such interaction should facilitate a cascade to longer waves which are vital for the DSA, not just for particle injection. Several hybrid simulations, addressing the acceleration efficiency of alpha particles, did include them self-consistently (Scholer et al. 1998, 1999; Burgess 1989; Trattner & Scholer 1991), however in some cases with *dramatically* reduced abundances (Caprioli et al. 2017), making them dynamically unimportant and thus completely excluding the He-driven waves. In Section 4.3 we further discuss the influence of these waves on energy spectra of proton and He ions. Besides, the earlier fully self-consistent simulations, facing the problem of injection of different ions (Caprioli et al. 2017), did not provide sufficiently detailed Mach number scans of the p/He injection ratio, that is needed to test the theoretically predicted p/He injection bias.

2. SIMULATION SET-UP

The full kinetic modeling of ion injection for a realistic ion-to-electron mass ratio m_i/m_e is challenging because of the necessity to resolve both the electron- and ion-scales. In this paper we study the particle injection into the DSA using hybrid simulations (Lipatov 2002, and references therein), where only the ion plasma population is treated kinetically, while electrons are treated as a charge neutralizing massless fluid. The hybrid simulations have been proven to be a powerful tool in the investigation of the non-relativistic shocks and have been used for a variety of problems (Lipatov 2002, and references therein), including the injection of

protons into the DSA process (Caprioli et al. 2015) and the study of the magnetic turbulence driven by plasma instabilities (Caprioli & Spitkovsky 2014). The underlying equations and implementation details are documented in the Appendix. The electron pressure p_e and the resistivity are both assumed to be isotropic quantities. The pressure p_e is modeled using an adiabatic equation of state with the adiabatic index $\gamma_e = 5/3$. The fluid equations and the ion equations of motion are non-relativistic, as $|\mathbf{v}| \ll c$ holds during the injection phase. In the simulations, lengths are given in units of c/ω_p , with $\omega_p = \sqrt{4\pi n_0 e^2/m_p}$ being the proton plasma frequency, n_0 the upstream density and e the proton charge. Time is measured in the units of inverse proton gyrofrequency, $\omega_c^{-1} = (e B_0/m_p c)^{-1}$. Here B_0 is the magnitude of the background magnetic field.

We use a realistic composition of the plasma consisting of ion species with number ratios corresponding to the amount of particles in the ISM. The fraction of ions respective to protons is $\sim 10\%$ for helium and $\sim 0.04\%$ for carbon and oxygen. Note, that He ions are dynamically important and cannot be regarded as test particles. The simulations are 1D in space but 3D in velocity and field components. This setting substantially increases the particle statistics and grid resolution, lowers the noise, and improves wave description, all being crucial for understanding the downstream thermalization. It is more important than possible shock rippling effects, not captured by 1D simulations. Besides that, shock rippling and its impact on particle reflection cannot be accurately characterized within hybrid simulations and require a full kinetic treatment (Liseykina et al. 2015; Malkov et al. 2016; Malkov 2017). For the reasons explained in detail in sections 4.2 and 4.3 we deliberately choose the 1D treatment as a first step in a systematic study of the A/Z dependence of injection efficiency. The follow up 2D simulations will be discussed elsewhere.

The simulation is initiated by sending a supersonic and superalfvénic plasma flow with velocity v_0 against a reflecting wall. The shock forms due to the interaction of the emerging counter-propagating flows. The background magnetic field is set parallel to the shock normal $\mathbf{B}_0 = B_0 \mathbf{x}$. The upstream plasma betas are $\beta_e = \beta_i = 1$. The simulation box has a length of $12 - 48 \cdot 10^3 c/\omega_p$, depending on the initial velocity v_0 . The spatial resolution of $\Delta x = 0.25 c/\omega_p$, 100 particles per species per numerical cell are used. The time step is $\Delta t = 0.01/(v_0/v_A) \omega_c^{-1}$ with $v_A = B_0/\sqrt{4\pi n_0 m_p}$. All numerical parameters have been checked for convergence.

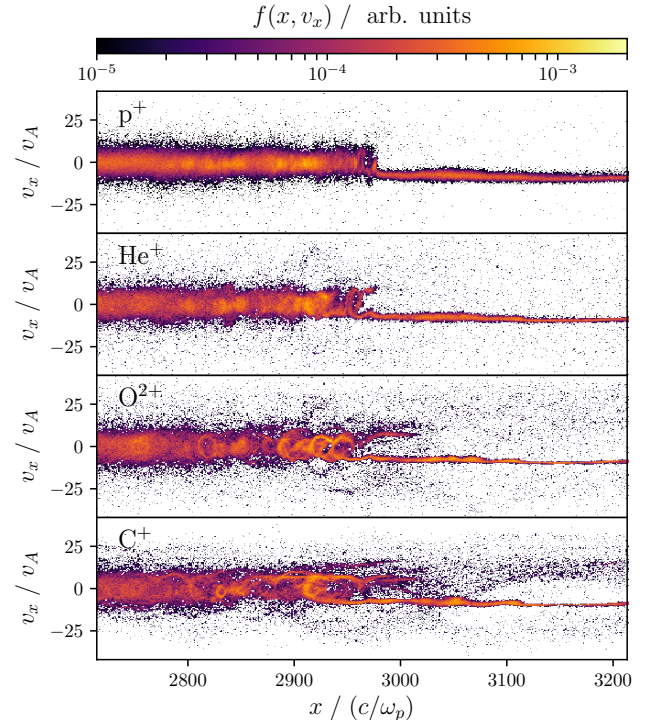


Figure 2. Phase space $f(x, v_x)$ for different ion species at $t = 1000 \omega_c^{-1}$. The plots show only a part of the simulation domain and are centered around the shock transition.

3. SIMULATION RESULTS

3.1. A/Z dependence of injection

We investigate the mass-to-charge dependence of the injection using self-consistent simulations for ion species with $A/Z \leq 16$. In addition to protons, He, C, and O ions with charge states $Z = 1$ and $Z = 2$ were included. The phase space distributions of selected ion species are shown in Fig. 2 for an upstream flow velocity $v_0 = 10 v_A$. The transition from the cold upstream flow to the hot and turbulent downstream plasma is clearly seen in the plots. The width of the particle distribution in v_x in the downstream is almost the same for all ion species, indicating higher temperatures for heavier species. The latter also thermalize further downstream as their impact from the shock is smoother. The presence of ions with large $|v_x|$ in the up- and downstream shows that some ions have already gained energy and are able to cross the shock front.

The energy spectra of the particles downstream of the shock transition at $t = 1500 \omega_c^{-1}$, obtained using a logarithmic binning procedure, are shown in Fig. 3a. The spectra of all ion species exhibit two main features: Maxwellian distribution and a power-law tail. The transition from the Maxwellian to the power-law tail is obscured by a contribution of suprathermal par-

ticles (Burgess & Scholer 2015). The spectra of heavier ions are shifted to higher energies, as the velocity is randomized during the shock crossing. For all species, α , the tail is clearly developed for energies $E > 10 E_0^\alpha$ with $E_0^\alpha = \frac{1}{2} m_\alpha v_0^2$. This energy is marked in the proton energy spectrum in Fig. 3a by the dashed gray line. After the spectra are converged ($t \geq 2000 \omega_c^{-1}$ for $v_0 = 10 v_A$), we calculate the selection rate, η_{sel} , i.e., the fraction of particles in the tail of the distribution function, as a function of mass-to-charge-ratio A/Z . For low A/Z , Fig. 3b, η_{sel} grows almost linearly, a saturation occurs around $A/Z \sim 8 - 12$ (in a *Mach-dependent fashion*, though) and at higher A/Z the selection rate decreases, recovering a physically correct $A/Z \rightarrow \infty$ asymptotic behavior (it should tend to zero, as for the injection of neutrals). The preliminary 2D simulations also evidence a deviation from the linear $\eta_{\text{sel}}(A/Z)$ trend, pointing towards a saturation for higher A/Z . Note, that the exact position of the saturation is to some extent time-dependent as heavier ions are accelerated at later times, Fig. 3c. This is because the respectively longer waves need to be generated by the increasing maximum energy of protons. The efficiency of these waves for injection of higher A/Z species naturally depends on their amplitudes. These amplitudes depend not only on the maximum momentum of (resonant) protons but also on the dynamics of the entire wave spectrum, i.e., spectral transfer rate, turbulent cascade, etc. Our $\eta_{\text{sel}}(A/Z)$ scaling (Fig. 3b) is in agreement up to $A/Z \leq 8$ with an almost linear increase of the selection rate with mass-to-charge ratio found recently in 2D hybrid simulations, facing the problem of injection of different ions in quasi-parallel shocks with $M > 5$ (Caprioli et al. 2017). For more extensive discussion about the behavior of η_{sel} for high values of A/Z , see Section 4.1.

3.2. Elemental selectivity: proton-to-helium ratio

In the following we investigate the elemental selectivity of the injection by focusing on the p/He ratio. To extract this quantity we calculate the injection efficiency of p and He^{2+} separately. The direct measurement of the injection efficiency is difficult, because the transition from the Maxwellian distribution to the power-law tail is not sharp. Therefore, we fit a thermal distribution $f_{\text{th}} \propto E^{1/2} \exp(-E/T)$ as well as a power-law with a cut-off, $f_{\text{pow}} \propto E^{-q} \exp(-E/E_{\text{cut}})$ to the low and high energy parts of the downstream spectrum. Here T is the downstream temperature of the respective ion species and E_{cut} is the cut-off energy. In Fig. 3a the dotted line denotes the fitted Maxwellian, while the dashed line is the power-law fit to the energy spectrum of protons. With E_{inj} defined for each species

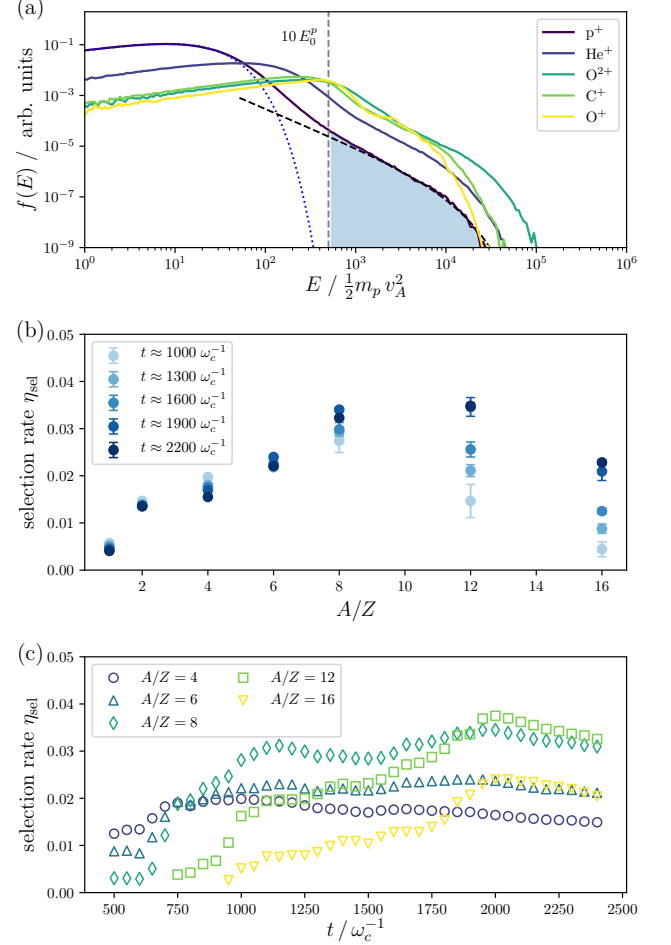


Figure 3. (a) Downstream energy spectra at $t = 1500 \omega_c^{-1}$ for selected ion species present in the simulation. The protons are in the tail of the distribution function if their energy exceeds $10 E_0^p$ (dashed gray line). The shaded area denotes the part of the spectrum, used for calculating the selection rate. (b) Selection rate η_{sel} as function of the mass-to-charge ratio for $v_0 = 10 v_A$, measured at different times between $t = 1000 \omega_c^{-1}$ and $t = 2200 \omega_c^{-1}$. (c) Selection rate as a function of time for selected ion species. The measurement of η_{sel} for heavy species with $A/Z > 6$ for $t < 1000 \omega_c^{-1}$ is not precise, because at this time the power tail of the distribution function is not yet well developed. Temporal evolutions $\eta_{\text{sel}}(t)$ shows how the time at which η_{sel} saturated depends on A/Z .

from $f_{\text{th}}(E_{\text{inj}}) = f_{\text{pow}}(E_{\text{inj}})$ the injection efficiency is calculated as

$$\eta_{\text{inj}} \propto \left. \frac{dN}{dE} \right|_{E=E_{\text{inj}}} = \frac{f_{\text{th}}(E_{\text{inj}})}{\int_0^\infty f_{\text{th}}(E) dE}. \quad (4)$$

Figure 4 shows the value of $\eta_{\text{inj}}^\alpha(M)$ obtained from a series of simulations with different initial upstream flow velocities v_0 . The corresponding Alfvénic shock Mach numbers are $M = (v_0 + v_s)/v_A$. Here v_s is the shock

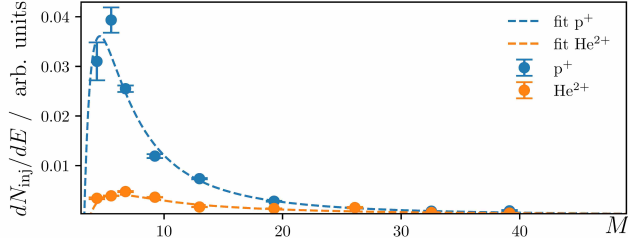


Figure 4. Injection efficiencies of protons and He^{2+} obtained from the simulation according to Eq. (4) as a function of Mach number. The dashed lines are the fits $\eta_{\text{inj}}(M) = a(M - b)M^{-c}$, with parameters $a_p = 5.68$, $b_p = 3.27$, $c_p = 3.50$, and $a_{\text{He}} = 0.25$, $b_{\text{He}} = 3.79$, $c_{\text{He}} = 2.73$.

velocity in the downstream rest frame. The M -dependence of η_{inj} is similar for p and He^{2+} . It increases for $M \lesssim 5$ for protons, $M \lesssim 7$ for He ions and decreases at higher M , tending to the predicted (Malkov 1998) $\eta_{\text{inj}}(M) \sim \ln M/M$ asymptotics.

Two aspects are important here. First, the injection of protons dominates for low M with η_{inj}^p exceeding the value of $\eta_{\text{inj}}^{\text{He}}$ by an order of magnitude. Second, the maximum of η_{inj}^p is shifted towards smaller M compared to He^{2+} . The prevalence of proton injection at weak shocks is also noticeable in the downstream temperature ratio T_{He}/T_p , which for $M < 15$ exceeds the expected ratio of $T_{\text{He}}/T_p = 4$.

3.3. Rigidity spectra

To model the time-dependent CR acceleration we combine the Mach number dependent injection efficiency obtained from simulations, Fig. 4, with the theoretical spectral slope, $q = 4/(1 - M^{-2})$ that allows us to extend the simulation spectra far beyond in rigidity that any simulation may possibly reach. The extension is justified by simulation spectra reaching the asymptotic DSA power-law, Fig. 3a.

During Sedov-Taylor phase of the SNR evolution the shock radius increases with time as $R_s \simeq C_{\text{ST}} t^{2/5}$, while the shock velocity decreases as $V_s \simeq (2/5) C_{\text{ST}} t^{-3/5}$, with $C_{\text{ST}} \simeq (2 E_e / \rho_0)^{1/5}$. Here E_e is the ejecta energy of the supernova, ρ_0 is the ambient density. The number of CR species α , deposited in the shock interior, as the shock radius increases from R_{min} to R_{max} , amounts to

$$N_\alpha(p) \propto \int_{R_{\text{min}}}^{R_{\text{max}}} f_\alpha(\mathcal{R}, M(R)) R^2 dR \propto \int_{M_{\text{max}}^{-2}}^{M_{\text{min}}^{-2}} f_\alpha(\mathcal{R}, M) dM^{-2}. \quad (5)$$

The spectra f_α are

$$f_\alpha \propto \eta_{\text{inj}}^\alpha(M) (\mathcal{R}/\mathcal{R}_{\text{inj}})^{-q(M)} \quad (6)$$

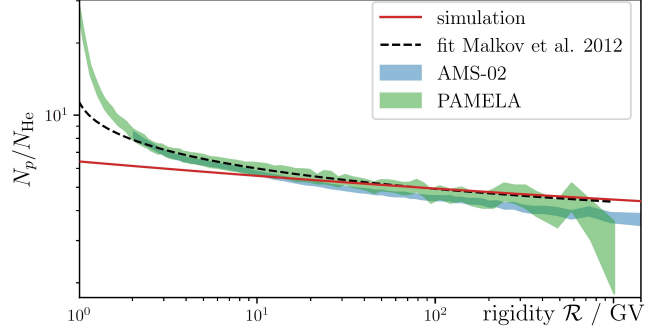


Figure 5. Proton-to-helium ratio as a function of particle rigidity. The results from the simulation (red line) are compared to the PAMELA and AMS-02 data. For details of the fit (dashed line) see Fig. 3 in Malkov et al. (2012). The observed p/He ratio is accurately reproduced in the range $\mathcal{R} \gtrsim 10$ GV.

with $q(M) = 4/(1 - M^{-2})$. Eqs. (5) and (6) are accurate for the most interesting sub-TV particles that are accelerated quickly. Eq. (5), however, tacitly imply an unimpeded release of accelerated particles into the ISM which is poorly known. The key to our approach is that p/He ratio is still independent of the release mechanism and even ensuing propagation across the ISM, simply because the underlying equations of motion are identical for p and He.

Instead of feeding the simulation data for $\eta_{\text{inj}}^\alpha(M)$ to the convolution given by Eqs. (5) and (6) we first fit the following simple function $\eta_{\text{inj}}(M) = a(M - b)M^{-c}$ in the range $M_{\text{min}} = 3.5 < M < M_{\text{max}} = 100$ to the data extracted from the simulations, Fig. 4, and then calculate the p/He ratio, N_p/N_{He} , according to Eq. (5), as a function of rigidity. The resulting p/He spectrum (red line), shown in Fig. 5, compares well in the high-rigidity range with the AMS-02 and PAMELA data (shadow areas).

4. DISCUSSION

4.1. A/Z trend of the selection rate

Our simulations show, Fig. 3 (b), that selection rate η_{sel} growth with mass-to-charge ratio, saturates in a Mach-dependent fashion around $A/Z \sim 8 - 12$, and then decreases for higher A/Z values, recovering a physically correct $A/Z \rightarrow \infty$ asymptotic behavior, as expected for neutral particles. However, this result is in contradiction with the findings recently reported in (Caprioli et al. 2017), where the authors have obtained in 2D hybrid simulations the quadratic growth with A/Z of the chemical enhancement for mass-to-charge ratios as high as $A/Z = 56$. The striking contradiction consists in the fact, that the quadratic growth of the chemical enhancement implies the linear growth of the se-

lection rate with A/Z *without trend to saturation* up to at least $A/Z = 56$. The question to address is then, whether the injection rate saturates and vanishes with growing A/Z or, on the contrary, the accelerated *protons* generate such strong and long waves and/or magnetized eddies downstream that they scatter and inject species with $A/Z \gg 1$ more efficiently than (“reductio ad absurdum”) the *protons* themselves. We stand by the statement, that the unlimited growth of the selection rate with A/Z is unphysical or, at a minimum, imposes quite unusual constraints on the scattering turbulence. It is worth mentioning, that the chemical enhancement of heavier elements with $A/Z > 8$ in Caprioli et al. (2017) is determined in the upstream plasma, because at time of measurement these ion species have not yet developed the universal downstream DSA spectrum. Whether this approach is justified at first place is controversial. The question of the exact position of maximum of η_{sel} as function of A/Z is debatable and there is indeed no consensus yet. Physically, its position should also depend on the current maximum energy of protons since resonant waves produced by them may scatter particles with larger A/Z . But the particle scattering rate in general decays with the growing wave length, so this effect should not be overestimated.

CR abundances of heavier elements, such as iron, have a weaker comparative potential for the verification of the A/Z scaling of injection efficiency than the rigidity spectra of p/He , p/O , p/C used in this paper. The reasons are of two kinds; first, there are not yet rigidity spectra of the ratios of heavier elements comparable in quality to the recently published AMS-02 data for the above ratios. The integrated abundancies are available, but they are affected by many factors either unrelated to the microphysics of injection selectivity in collisionless shocks or highly uncertain. These include, but are not limited to, CR spallation effects during the propagation to the Earth, the possible contribution from the disintegration of dust grains, and the uncertainty in the ionization state during the injection process.

4.2. Do 2D simulations produce more credible results?

Although most fundamental aspects of shocks are one-dimensional, there are indeed essential phenomena that cannot be fully understood if two or even just one coordinate is ignored. Obviously, realism demands to trade the fully 3D simulations for an adequate resolution. In the case of hybrid simulations this requirement concerns both the particle statistic and parameters of the numerical grid. Despite the progress in computational performance, the 3D simulations meeting such conditions are hardly possible now, therefore 2D modeling appears as

a computationally expensive, but a plausible compromise. With this it is tacitly assumed that 2D simulations of collisionless shock particle acceleration produce more credible results than 1D simulations do. However, there are well-known aspects of particularly the 2D fluid Kraichnan (1967); Weiss (1991); Biskamp & Welter (1989), absent in 3D, that makes the preponderance of 2D over 1D modeling questionable for the studies of particle scattering and acceleration.

First, an inverse cascade in 2D fluid leads to coherent structures that may become responsible for an excessive particle scattering and reflection, i.e. *injection*. Although the difference between 2D and 3D dynamics is not so explicit in the MHD, the conditions and the character of an inverse cascade in 3D MHD are not so robust as in the 2D case (Pouquet et al. 1976).

Second, high computational demands of injection studies force to elongate the simulation box significantly in the shock normal direction which is unnatural for a shock alignment along its front. The small transverse box size renders the 2D simulations quasi one-dimensional, but an artificial scale introduced by it can cause an artificial periodicity for ions with large Larmor radii and is likely to determine the size of the scattering structures (Ngan et al. 2005; Celani et al. 2010), shock corrugation scale, and the inverse cascade anisotropy. Structures that appear to be strongly influenced by the box geometry are seen in some advanced 2D simulations, e.g., (Caprioli & Spitkovsky 2013). They would, perhaps, be acceptable for a shock tube setting, but problematic for a freely propagating shock front.

Third, besides their exaggerated magnetic strength, coherent structures in the 2D downstream turbulence are highly consequential for the particle injection for another reason as well: as the particle motion is considered three-dimensional, these structures, being extended along the ignorable coordinate, dramatically increase the effective scattering cross-section for particles. The particles are scattered by these structures regardless of their velocity projection on the ignorable coordinate. In a square box of size L^2 and the typical scale of the scattering structure $\sim a$, this enhancement is a factor of $L/a \gg 1$, compared to the 3D box L^3 . Such particle dynamics may indeed result in an excessive return upstream of particles with high A/Z , that would in 3D pass through these structures, not to mention the uncertainty of their formation in the 3D.

4.3. Importance of the He-driven waves

Besides already stated, the peculiarity of our study is in the interaction of the shock with a large number of different species for which adequate particle statistics

is vital, especially when exploring the high-energy tails of the distribution functions. As we briefly discussed in the Introduction, Sec. 1, the He-driven waves significantly enrich the wave spectrum by their parametric interaction with the proton-driven waves, thus facilitating particle thermalization downstream. Because of the high computational demand in the 2D hybrid numerical studies of injection, the heavier ions, including He, are either treated as test-particles, or included quasi-self-consistently with low statistic and an extremely low abundance. The latter protects the hybrid simulations from an excessive numerical heating, which otherwise would unavoidably represent a serious problem, but at the same time completely excludes the generation of the He-driven waves, by making He-component dynamically unimportant. In Fig. 6a the spectrum of the transverse magnetic field $\mathcal{F}[B_y](k)$ in a two-ion species (90% protons and 10% He²⁺) plasma is shown for $t = 500\omega_c^{-1}$ in comparison with the corresponding spectrum in a pure hydrogen plasma. If the abundance of He²⁺ component is high, a component at lower wave-number k appears in the spectrum (shown by an arrow). The critical role of the self-consistent, as opposed to test-particle, treatment of He²⁺ population is confirmed by the enhanced number of downstream protons with high energies and an increase in the number of helium ions near the cut-off (Fig. 6b). In general, DSA is a bootstrap process, in which the particles with high energy drive longest waves that help to accelerate them. Here helium paves the way for protons. The well established part of the He spectrum is in turn dominated by more abundant protons in both cases.

5. SUMMARY

We investigate the particle injection into the DSA using self-consistent hybrid simulations. We provide sufficiently detailed Mach number scans of the p/He injection *ratio*, that is needed to test the injection bias. It should be emphasized that the rigidity spectra of the *fractions* of different species do not depend on the relation, in which these elements are in the most productive SNRs, as protons are considered to be dynamically

most important species. The reduced spatial dimensionality of the simulations allows us to increase the particle statistics and grid resolution dramatically. Our simulations show that selection rate of different ion species increases with A/Z , saturates, and peaks as a function of Mach number. They correctly predict the decrease in proton-to-helium ratio with increasing rigidity, Fig. 5, at almost exactly the rate $\Delta q \approx 0.1$, measured in the experiments for $\mathcal{R} \gtrsim 10$ GV. At lower rigidities, the difference between the data and our predictions is significant. Based on the discussion made in the introduction, the difference *must* occur because the equations of motion, Eqs. (1), (2), for protons and helium ions deviate toward lower rigidities. The most likely cause of this deviation is particle interaction with the turbulent solar wind in the Heliosphere, but the interaction with the ISM turbulence may also contribute, again, because the equations of motion are different for p and He in the low-rigidity range. By contrast, the deviation from the AMS-02 data in the high-rigidity range, where the equations of motion for p and He become identical, is insignificant as expected. This deviation is much less than the difference $\Delta q \approx 0.1$. Whether it comes from a simplified integration over the SNR in Eqs. (5) and (6) or it is a mixing effect from different SNRs or spallation in the ISM, remains unclear. The difference is small enough to be accounted for by any of these phenomena. Except for this uncertainty, the suggested mechanism for A/Z -dependence of the injection fully explains the measured p/He ratio. Our interpretation of the elemental "anomaly" is therefore intrinsic to collisionless shock mechanisms and does not require additional assumptions, such as the contributions from several different SNRs, their inhomogeneous environments or acceleration from grains.

The research was supported by the DFG within the Research grant 278305671, by RSF 16-11-10028, and by NASA ATP-program within grants NNX14AH36G and 80NSSC17K0255. Simulations were performed using the computing resources granted by the North-German Supercomputing Alliance (HLRN) under the project mvp00015.

APPENDIX

In hybrid modelling the evolution of the ion distribution function f is governed by the kinetic Vlasov equation:

$$\frac{\partial}{\partial t} f + \mathbf{v}_i \nabla f + \frac{q_i}{m_i} \left(\mathbf{E} + \frac{1}{c} \mathbf{v}_i \times \mathbf{B} - \eta \mathbf{J} \right) \frac{\partial}{\partial v} f = 0. \quad (1)$$

Here \mathbf{E} and \mathbf{B} are the electric and magnetic fields and $\mathbf{J} = e(n_i \mathbf{v}_i - n_e \mathbf{v}_e) \approx en(\mathbf{v}_i - \mathbf{v}_e)$ is the current density. Furthermore, $q_i = Ze$ and $m_i = Am_p$ are the ion charge and mass and η denotes a scalar resistivity.

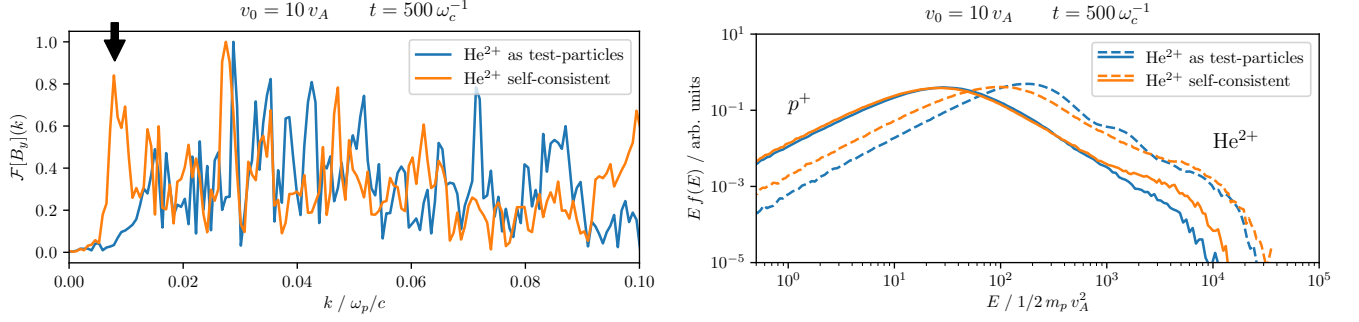


Figure 6. (left) Spectra of the magnetic field $\mathcal{F}[B_y](k)$ in the whole simulation box for simulations with a single-ion species (only protons self-consistent, He ions as test-particles) (blue) and a two-ion species (90% protons and 10% He ions) (orange) plasma. If He²⁺ population is present, a component at lower k appears in the spectra. (right) Downstream energy spectra of protons (solid line) and He²⁺ ions (dashed line) for simulations with a single species (100% protons) (blue) and a two-ion species (90% protons and 10% He ions) (orange) plasma. In the former case the He ions are treated as test-particles, that move in the fields, created by protons. The proton spectrum (solid line) differs only in the high energy part. Due to the longer waves, that are generated if helium is included self-consistently, more protons are accelerated to higher energies. For the energy spectrum of helium (dashed line) the main difference at $t = 500 \omega_c^{-1}$ is close to the cut-off, where some enhancement is evident and in the thermal part of the spectrum.

The plasma electrons on the other hand are treated as a charge neutralizing massless fluid,

$$n_e m \frac{d\mathbf{v}_e}{dt} = 0 = -e n_e \left(\mathbf{E} + \frac{1}{c} \mathbf{v} \times \mathbf{B} \right) - \nabla p_e + e n_e \eta \mathbf{J}. \quad (2)$$

Here p_e denotes the electron pressure, which can be calculated as $p_e = n k_B T$. In order to close the set of equations we assume an adiabatic equation of state

$$\frac{T_e}{T_0} = \left(\frac{n_e}{n_0} \right)^{\gamma-1} \quad \text{with: } \gamma = \frac{5}{3} \quad (3)$$

We found that the use a polytropic equation of state, as in e.g. (Caprioli et al. 2015), instead of an adiabatic one does not change the energy spectra significantly and the injection rate behavior for large A/Z is not affected by the prescription for the electron equation of state. Furthermore, an effective adiabatic index, based on the assumption of equilibration of electron and ion temperatures in the downstream might be justified for weak shocks, as (Vink, Jacco et al. 2015) predicts a thermalization between electrons and ions at low M shocks. However, at higher Mach numbers ($5 < M_s < 60$) the same authors predicted a behavior of $T_e/T_i \propto M_s^{-2}$. Hence the assumption of electron and ion temperature equilibration might not hold.

Furthermore, we use the low-frequency magnetostatic model, neglecting the displacement current in the Ampere's law.

A. Implementation

The particle-in-cell method is used for the ion plasma-components. A first order weighting is applied to interpolate the fields to the particle position, as well as to obtain ion current and charge density from the known positions of the ion-particles relative to the grid points. The *Boris-algorithm* (Boris & Shanny 1970) is used to update the particle positions and velocities. The magnetic field evolves according to Faraday's law, while the electric field is calculated from the electron momentum equation, Eq.(2). The equations of the evolution of the fields are discretized using second order finite difference stencils:

$$\begin{aligned} \mathbf{B}^{n+1/2} &= \mathbf{B}^n - \frac{\Delta t}{2} \nabla \times \mathbf{E}^n \\ \mathbf{E}^{n+1/2} &= F(\mathbf{B}^{n+1/2}, n_i^{n+1/2}, \mathbf{J}_i^{n+1/2}) \\ \mathbf{B}^{n+1} &= \mathbf{B}^{n+1/2} - \frac{\Delta t}{2} \nabla \times \mathbf{E}^{n+1/2} \end{aligned}$$

Technically, the problem of the time evolution of the fields reduces the problem of calculating \mathbf{E}^{n+1} , which cannot be calculated directly, since \mathbf{J}_i^{n+1} is not known. Several different methods have been proposed in the literature, see

(Winske et al. 2003) for a review. We use a predictor-corrector method, which is simple and has good energy conserving properties. The algorithm has the following steps:

1. advance \mathbf{B}^n and \mathbf{E}^n to the time step $n + 1/2$

$$\begin{aligned}\mathbf{B}^{n+1/2} &= \mathbf{B}^n - \frac{\Delta t}{2} \nabla \times \mathbf{E}^n \\ \mathbf{E}^{n+1/2} &= F(\mathbf{B}^{n+1/2}, n_i^{n+1/2}, \mathbf{J}_i^{n+1/2})\end{aligned}$$

2. predict fields \mathbf{B}'^{n+1} and \mathbf{E}'^{n+1}

$$\begin{aligned}\mathbf{E}'^{n+1} &= 2\mathbf{E}^{n+1/2} - \mathbf{E}^n \\ \mathbf{B}'^{n+1} &= \mathbf{B}^{n+1/2} - \frac{\Delta t}{2} \nabla \times \mathbf{E}'^{n+1}\end{aligned}$$

3. advance particles using the predicted fields and obtain $n_i'^{n+3/2}$ and $\mathbf{J}_p'^{n+3/2}$

4. calculate predicted fields $\mathbf{B}''^{n+3/2}$ and $\mathbf{E}''^{n+3/2}$

$$\begin{aligned}\mathbf{B}''^{n+3/2} &= \mathbf{B}'^{n+1} - \frac{\Delta t}{2} \nabla \times \mathbf{E}'^{n+1} \\ \mathbf{E}''^{n+3/2} &= F(\mathbf{B}''^{n+3/2}, n_i''^{n+3/2}, \mathbf{J}_i''^{n+3/2})\end{aligned}$$

5. determine \mathbf{B}^{n+1} and \mathbf{E}^{n+1}

$$\begin{aligned}\mathbf{E}^{n+1} &= \frac{1}{2} (\mathbf{E}''^{n+3/2} - \mathbf{E}^{n+1/2}) \\ \mathbf{B}^{n+1} &= \mathbf{B}^{n+1/2} - \frac{\Delta t}{2} \nabla \times \mathbf{E}^{n+1}.\end{aligned}$$

REFERENCES

- Abe, K., et al. 2016, *Astrophys. J.*, 822, 65
- Adriani, O., et al. 2011, *Science*, 332, 69,
doi: [10.1126/science.1199172](https://doi.org/10.1126/science.1199172)
- Aguilar, M., et al. 2015, *Phys. Rev. Lett.*, 115, 211101,
doi: [10.1103/PhysRevLett.115.211101](https://doi.org/10.1103/PhysRevLett.115.211101)
- . 2017, *Phys. Rev. Lett.*, 119, 251101,
doi: [10.1103/PhysRevLett.119.251101](https://doi.org/10.1103/PhysRevLett.119.251101)
- . 2018, *Phys. Rev. Lett.*, 120, 021101,
doi: [10.1103/PhysRevLett.120.021101](https://doi.org/10.1103/PhysRevLett.120.021101)
- Biskamp, D., & Welter, H. 1989, *Physics of Fluids B: Plasma Physics*, 1, 1964, doi: [10.1063/1.859060](https://doi.org/10.1063/1.859060)
- Boris, J. P., & Shanny, R. A. 1970, *Proceedings: Fourth Conference on Numerical Simulation of Plasmas*, November 2, 3, 1970 (Naval Research Laboratory)
- Burgess, D. 1989, *Geophys. Res. Lett.*, 16, 163,
doi: [10.1029/GL016i002p00163](https://doi.org/10.1029/GL016i002p00163)
- Burgess, D., & Scholer, M. 2015, *Collisionless shocks in space plasmas: structure and accelerated particles* (Cambridge University Press),
doi: <https://doi.org/10.1017/CBO9781139044097>
- Bykov, A. M., Ellison, D. C., Marcowith, A., & Osipov, S. M. 2018, *Space Science Reviews*, 214, 41,
doi: [10.1007/s11214-018-0479-4](https://doi.org/10.1007/s11214-018-0479-4)
- Caprioli, D., Pop, A.-R., & Spitkovsky, A. 2015, *Astrophys. J. Lett.*, 798, L28,
doi: <https://dx.doi.org/10.1088/2041-8205/798/2/L28>
- Caprioli, D., & Spitkovsky, A. 2013, *Astrophys. J. Lett.*, 765, L20, doi: [10.1088/2041-8205/765/1/L20](https://doi.org/10.1088/2041-8205/765/1/L20)
- . 2014, *The Astrophysical Journal*, 794, 46
- Caprioli, D., Yi, D. T., & Spitkovsky, A. 2017, *Phys. Rev. Lett.*, 119, 171101,
doi: [10.1103/PhysRevLett.119.171101](https://doi.org/10.1103/PhysRevLett.119.171101)
- Celani, A., Musacchio, S., & Vincenzi, D. 2010, *Phys. Rev. Lett.*, 104, 184506,
doi: [10.1103/PhysRevLett.104.184506](https://doi.org/10.1103/PhysRevLett.104.184506)
- Fermi, E. 1949, *Phys. Rev.*, 75, 1169,
doi: [10.1103/PhysRev.75.1169](https://doi.org/10.1103/PhysRev.75.1169)
- Kato, T. N. 2015, *Astrophys. J.*, 802, 115,
doi: <https://doi.org/10.1088/0004-637X/802/2/115>
- Kraichnan, R. H. 1967, *Physics of Fluids*, 10, 1417,
doi: [10.1063/1.1762301](https://doi.org/10.1063/1.1762301)

- Lipatov, A. S. 2002, *The Hybrid Multiscale Simulation Technology. An Introduction with Application to Astrophysical and Laboratory Plasmas* (Springer, Berlin, Heidelberg). <https://doi.org/10.1007/978-3-662-05012-5>
- Liseykina, T., Dudnikova, G., Vshivkov, V., & Malkov, M. 2015, *J. Plasma Phys.* , 81, doi: [10.1017/S002237781500077X](https://doi.org/10.1017/S002237781500077X)
- Malkov, M. A. 1998, *Phys. Rev. E* , 58, 4911, doi: [10.1103/PhysRevE.58.4911](https://doi.org/10.1103/PhysRevE.58.4911)
- Malkov, M. A. 2017, in 2nd Conference on Cosmic Ray Origin - beyond the standard models San Vito di Cadore, Dolomites, Italy, September 18-24, 2016. <https://inspirehep.net/record/1518114/files/arXiv:1703.05772.pdf>
- Malkov, M. A., Diamond, P. H., & Sagdeev, R. Z. 2012, *Phys. Rev. Lett.* , 108, 081104, doi: [10.1103/PhysRevLett.108.081104](https://doi.org/10.1103/PhysRevLett.108.081104)
- Malkov, M. A., Sagdeev, R. Z., Dudnikova, G. I., et al. 2016, *Physics of Plasmas* , 23, 043105, doi: [10.1063/1.4945649](https://doi.org/10.1063/1.4945649)
- Malkov, M. A., & Völk, H. J. 1995, *Astronomy and Astrophys.*, 300, 605
- Marcowith, A., Bret, A., Bykov, A., et al. 2016, *Reports on Progress in Physics*, 79, 046901, doi: <https://doi.org/10.1088/0034-4885/79/4/046901>
- Ngan, K., Straub, D. N., & Bartello, P. 2005, *Physics of Fluids* , 17, 125102, doi: [10.1063/1.2139685](https://doi.org/10.1063/1.2139685)
- Ohira, Y., & Ioka, K. 2011, *Astrophys. J. Lett.* , 729, L13, doi: <https://link.aps.org/doi/10.1088/2041-8205/729/1/L13>
- Ohira, Y., Kawanaka, N., & Ioka, K. 2016, *Phys. Rev. D*, 93, 083001, doi: [10.1103/PhysRevD.93.083001](https://doi.org/10.1103/PhysRevD.93.083001)
- Panov, A. D., et al. 2009, *Bulletin of the Russian Academy of Sciences: Physics*, 73, 564, doi: [10.3103/S1062873809050098](https://doi.org/10.3103/S1062873809050098)
- Parker, E. N. 1961, *Journal of Nuclear Energy*, 2, 146
- Pouquet, A., Frisch, U., & Lortat, J. 1976, *Journal of Fluid Mechanics*, 77, 321354, doi: [10.1017/S0022112076002140](https://doi.org/10.1017/S0022112076002140)
- Quest, K. B. 1988, *J. Geophys. Res.* , 93, 9649, doi: <https://dx.doi.org/10.1029/JA093iA09p09649>
- Scholer, M., Kucharek, H., & Trattner, K. 1998, *Advances in Space Research*, 21, 533 , doi: [https://doi.org/10.1016/S0273-1177\(97\)00958-7](https://doi.org/10.1016/S0273-1177(97)00958-7)
- Scholer, M., Kucharek, H., & Trattner, K.-H. 1999, *Annales Geophysicae*, 17, 583
- Serpico, P. D. 2016, *PoS, ICRC2015*, 009. <https://arxiv.org/abs/1509.04233>
- Trattner, K. J., & Scholer, M. 1991, *Geophys. Res. Lett.* , 18, 1817, doi: [10.1029/91GL02084](https://doi.org/10.1029/91GL02084)
- Vink, Jacco, Broersen, Sjors, Bykov, Andrei, & Gabici, Stefano. 2015, *Astronomy and Astrophys.*, 579, A13, doi: [10.1051/0004-6361/201424612](https://doi.org/10.1051/0004-6361/201424612)
- Vladimirov, A. E., Jóhannesson, G., Moskalenko, I. V., & Porter, T. A. 2012, *Astrophys. J.* , 752, 68, doi: <https://dx.doi.org/10.1088/0004-637X/752/1/68>
- Weiss, J. 1991, *Physica D Nonlinear Phenomena*, 48, 273, doi: [10.1016/0167-2789\(91\)90088-Q](https://doi.org/10.1016/0167-2789(91)90088-Q)
- Winske, D., Yin, L., Omid, N., Karimabadi, H., & Quest, K. 2003, *Hybrid Simulation Codes: Past, Present and Future—A Tutorial*, ed. J. Büchner, M. Scholer, & C. T. Dum (Berlin, Heidelberg: Springer Berlin Heidelberg), 136–165
- Yoon, Y. S., et al. 2011, *Astrophys. J.* , 728, 122, doi: <https://dx.doi.org/10.1088/0004-637X/728/2/122>